Damping numerical oscillations in hybrid solvers through detection of Gibbs phenomenon

V. Kalyana Chakravarthy*,† and D. Chakraborty

*Defence Research and Development Laboratory, Defence Research and Development Organisation, Kanchanbagh,
Hyderabad 500058, India*

SUMMARY

A Gibbs phenomenon detector that is useful in damping numerical oscillations in hybrid solvers for compressible turbulence is proposed and tested. It is designed to function in regions away from discontinuities where commonly used discontinuity sensors are ineffective. Using this Gibbs phenomenon detector in addition to a discontinuity sensor for combining central and shock capturing schemes provides an integrated way of dealing with numerical oscillations generated by shock waves and contact lines that are normal to the flow. When complete suppression of numerical oscillations is not possible, they are sufficiently localized. Canonical tests and large eddy simulations show that inclusion of the proposed detector does not cause additional damping of 'well-resolved' physical oscillations. Copyright © 2017 John Wiley & Sons, Ltd.

1. INTRODUCTION

Hybrid solvers for simulating compressible turbulence rely on non-dissipative schemes for capturing turbulence while switching to dissipative schemes in the vicinity of discontinuities [1, 2]. Recent state-of-the-art high-fidelity numerical simulations of supersonic turbulent flows involving shocks [3] rely on the use of energy-consistent methods based on a central, locally conservative discretization of the convective terms cast in skew-symmetric form. Shock capturing is then accomplished by hybridization with a dissipative (typically weighted essentially non-oscillatory (WENO)) scheme strictly applied around discontinuities. The use of dissipative schemes should be localized appropriately. The use of dissipative scheme over a broader region around discontinuities leads to undesirable dissipation of physical oscillations, while extreme localization leads to numerical oscillations that persist for long distances. If proper localization is not possible, another mechanism is needed to remove oscillations away from discontinuities.

Oscillations away from discontinuities are not unique to hybrid approaches. Hyperviscosity approaches that are often implemented using central compact schemes resort to higher-order spectral/compact/dealisaing filtering [4] sometimes in addition to smoothing of hyperviscosity computed using polyharmonic operators to deal with this problem [4, 5]. Approaches based on characteristic filtering built using compact schemes [6] also need additional higher-order filtering steps unless the base scheme itself is upwinded [7]. Finally, the explicit filtering approaches also rely on two filters [8]: one which is ubiquitous and the other localized. Only pure WENO schemes are immune to this problem, but they have been deemed [9, 10] too dissipative to capture turbulence accurately.

---

*Correspondence to: V. Kalyana Chakravarthy, Defence Research and Development Laboratory, Defence Research and Development Organisation, Kanchanbagh, Hyderabad 500058, India.
†E-mail: v_kalyana_chakravarthy@yahoo.co.in

A simple and effective way of dealing with numerical oscillations in hybrid, explicit finite volume schemes by basing the weights on a Gibbs phenomenon detector in addition to a more traditional discontinuity sensor was proposed earlier and studied using canonical problems [11]. The present work differs from an earlier study in two ways.

First, the Rotated Harten, Lax and van Leer (RHLL) solver [12] is used for capturing shocks/contact lines here, while the earlier work was based on the SLAU2 scheme [13, 14]. Both these schemes can resolve contact lines without odd–even instability. This ability of RHLL comes from a combination of Roe and HLL solvers. While it provides crisper resolution of shocks than SLAU2, problems could arise when this compound scheme is further combined with a central scheme to formulate a hybrid scheme for compressible turbulence. This effort checks for such unforeseen problems. The general applicability of the approach independent of shock capturing scheme is also verified to a degree in the process.

The earlier work demonstrated hybridization for canonical problems that serve as prototypes for actual turbulent flows. The validation was also mostly qualitative. No DNS or LES were reported. In the present work, two LES are reported. The results are compared with published LES results, and the effectiveness of the new approach over use of just a conventional discontinuity sensor is checked. The new approach seems to be of less consequence in the first LES than the second, and the reasons are discussed.

2. NUMERICAL METHOD

An explicit second-order Runge–Kutta scheme is used for temporal integration of the governing equations. The net flux on a cell face is computed as follows:

$$F_h = \theta F_c + (1 - \theta) F_u \tag{1}$$

F_c and F_u are the centered and upwind fluxes computed, respectively, using fourth-order Mac-Cormack and second-order RHLL [12] schemes. The MacCormack scheme is apt because it is the simplest non-dissipative scheme that does not need artificial dissipation or special care like the Rhie–Chow correction [15] for preventing checkerboard-type oscillations on non-staggered meshes. Fourth-order spatial accuracy is achieved by interpolating fluxes computed at cell centers to faces using stencils proposed by Genin [2]. F_u is computed using the RHLL scheme developed by Nishikawa and Kitamura [12]. It captures shock and contact discontinuities crisply without suffering from carbuncle phenomenon or the odd–even instability.

The following discontinuity sensor proposed by Genin [2] is used here because it can detect contact lines in addition to shock waves.

$$
\begin{aligned}
S_{\phi,i} &= \frac{|\phi_{i+1} - 2\phi_i + \phi_{i-1}|}{|\phi_{i+1} - \phi_i| + |\phi_i - \phi_{i-1}|}, if \, |\phi_{i+1} - 2\phi_i + \phi_{i-1}| \geqslant \epsilon_\phi \phi_i \\
&= -S_\phi^{th}, \text{otherwise}
\end{aligned}
\tag{2}
$$

$$S_{i+1/2} = \max(S_{P,i}, S_{P,i+1}, S_{\rho,i}, S_{\rho,i+1}) \tag{3}$$

The constants ϵ_P and ϵ_ρ for pressure and density fields were set to 0.05 and 0.1, while the corresponding threshold values S_P^{th} and S_ρ^{th} equal to 0.5 and 0.25, respectively.

Genin [2] used a Heaviside function of smoothness parameter to arrive at the weights in Equation (1).

$$\theta_{old} = 1 - H(S) \tag{4}$$

The discontinuity sensor activates the flux splitting scheme only near shocks and contact lines. The proposed approach seeks to additionally suppress two-point oscillations that may not be right next to the discontinuities. These oscillations could result from discontinuity sensor-based hybridization as in the aforementioned equation (i.e., shift from a central scheme elsewhere to a shock capturing scheme near shocks) or have other origins as in an example problem later.

First, the Gibbs phenomenon is detected as follows:

$$S'_{i+1/2} = \frac{(\rho_{i+2} - 2\rho_{i+1} + \rho_i)(\rho_{i+1} - 2\rho_i + \rho_{i-1})}{(\rho_{i+1} - \rho_i)^2} \tag{5}$$

Extrema could actually exist in solutions of Euler equations, but existence of local maxima and minima right next to each other on the computational grid is an unphysical artifact. At such locations, the value of S' is negative. Shock capturing schemes are generally monotone by design, that is, they do not result in any new extrema. By increasing the weight for the shock capturing scheme in the presence of such numerical artifacts, it may be possible to suppress the creation of the two-point oscillations.

$$\theta_{\text{new}} = \min\left[\frac{1}{1 + \exp(14S)}, \exp(\min(2.5S', 0.0))\right] \tag{6}$$

In addition to considering S' in determining the weights, the discontinuity sensor has also been modified by smoothing the discontinuity sensor in Equation (4) with $1/[1 + \exp(14S)]$. The idea is that more gradual changes in weights across a discontinuity might lead to smaller numerical oscillations.

So the switching function is now calculated as a function of both S, the shock or contact discontinuity sensor, and S', the Gibbs phenomenon detector. As in other alternate approaches [5, 9, 10, 16, 17], there are numerical constants involved in this procedure. The values shown in the aforementioned equation, however, seem to work in all of the test cases including some that have been left out here.

3. RESULTS

Four canonical problems are considered here before testing the proposed modification in a large eddy simulations. Physical oscillations are not present in two of the problems, while in others, they are generated because of the interaction of shocks with spatially varying density or vorticity fields. The physical oscillations have to be captured where necessary without generating numerical ones.

3.1. Shu–Osher test

This problem involves a Mach 3 shock moving through a sinusoidally varying density field leaving behind physical oscillations. Predictions of the proposed hybrid method on a 400-point mesh (like
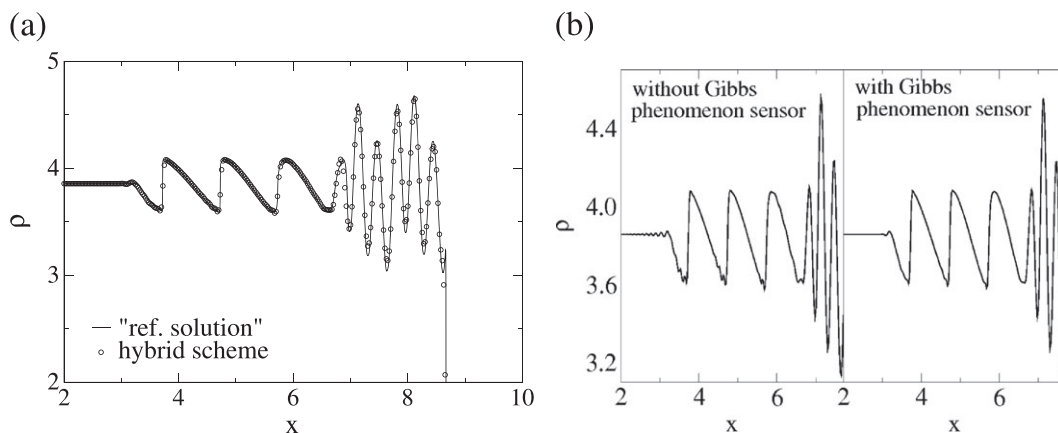

Figure 1. (a) Comparison of predicted density variation with reference solution. (b) Effect of using the Gibbs phenomenon sensor.

in previous studies [2, 7, 16, 18]) are compared with a reference high-resolution solution (computed using the shock capturing scheme on a 32,000-point mesh) Figure 1(a) and with a solution computed with weights based on only the discontinuity sensor in Figure 1(b). The use of Gibbs phenomenon detector seems to suppress not only two-point oscillations but also numerical oscillations of higher wavelength that probably arise as the solver responds to the former. The physical oscillations, however, remain unaffected.

3.2. Axisymmetric blast wave

A two-dimensional circular blast wave problem proposed by Toro [19] is chosen as the second test case. This, in a way, is an axisymmetric counterpart of the Sod's shock tube problem, and so additional demonstration on the latter is not needed. Further, it involves a contact discontinuity that is not present in Noh's test problem [9]. The initial density and pressure are both set to unity inside a circle of radius of 0.4, while they equal 0.125 and 0.1 units outside (gas constant is set to unity). A quarter of the problem is simulated for time of 0.25 units by discretizing a unit square domain with a 400×400 mesh [18]), and density isolevels are plotted in Figure 2(a) in order to facilitate comparison with results from a comparative study of Liska and Wendroff [18]. In this study, all schemes retained the axisymmetric nature of the shock wave but not the contact line. An early version of WENO predicted a crisp contact line but was susceptible to numerical instabilities that produced unphysical wiggles when the contact line was aligned to grid directions. High-resolution schemes like the piecewise parabolic methods also produced unphysical wiggles but with less directional dependency. The present hybrid scheme predicts a more circular contact line with less directional dependency and smaller unphysical wiggles. The effect of including the new sensor in hybridization is illustrated in Figure 2(b). The hybridization generates a post shock kink in density followed by numerical oscillations. By using the Gibbs phenomenon detector, these oscillations are eliminated, but a localized artifact in the form of a density kink, although diminished, remains. This is also a feature of hyperviscosity approaches (as seen in solutions for the Shu–Osher test). Note that the kink is reduced considerably when the RHLL scheme is used instead of the SLAU2 scheme [11].

3.3. Emery test case: supersonic flow over a forward-facing step

This flow [20] has many interacting waves and is a good test case for testing hybrid solvers. It involves simulating the response of inviscid Mach 3 flow in a 3×1 sized channel to sudden introduction of a forward-facing step at location $x = 2$. Most of the artifacts associated with shock capturing schemes, like carbuncle phenomena, odd–even instability, if present, would be evident

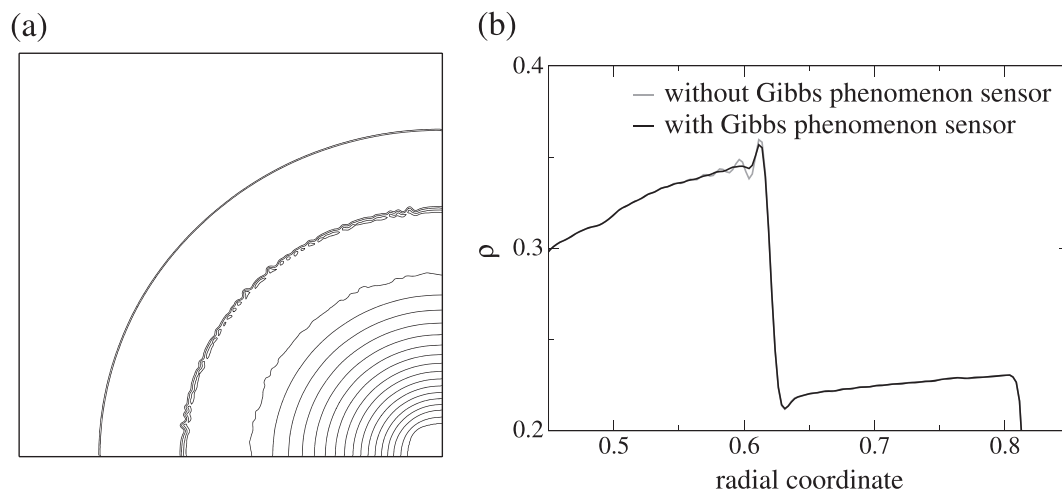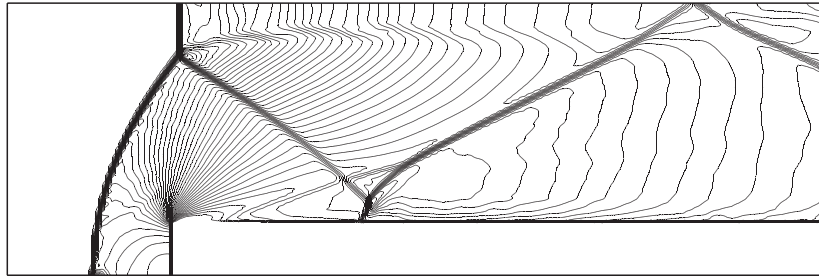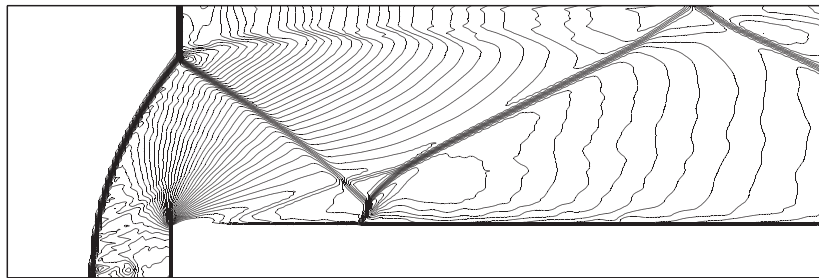(a)   (b)

Figure 2. (a) Predicted density isolevels for Toro's blast wave problem. (b) Effect of using the Gibbs phenomenon sensor on radial density variation.

(a) with Gibbs phenomenon detector

(b) without Gibbs phenomenon detector

Figure 3. Density isolevels for the Emery test problem.

from the density isolevels plot [14]. The density isolevels predicted with (using Equation (6)) and without (Equation (4)) using the Gibbs phenomenon detector on a 240×80 mesh are compared in Figure 3. Without the Gibbs phenomenon detector, switching generates unphysical oscillations behind the leading shock wave. They are to a large extent suppressed if this detector is activated. It is also to be noted that the two simulations predict identical results around the two slip lines. First one is generated at the shock triple point, while the second is generated at the convex corner of the step. There are no unphysical jumps in density field next to the contact lines like in the case of the blast wave problem. This problem seems to come up only when the contact lines are normal (and perhaps at a non-zero angle) to the flow direction. If the contact lines are aligned with the flow, there does not seem to be a problem in using the hybrid solvers.

3.4. Shock interaction with a single vortex

Compressible turbulence involves interaction of shocks with density/entropy fluctuations (as in the Shu–Osher problem) and vorticity fields. Shock interaction with a single vortex [6, 7] is simulated here on a uniform 250×100 mesh. An isentropic compressible vortex centered initially at [0.25, 0.5] is convected into a stationary Mach 1.1 shock located at $x = 1$ in a $[0, 2] \times [0, 1]$ domain. The parameters of this test case are available from several previous studies and not repeated here. Comparison of density isolevels in Figure 4 indicates that post-shock oscillations that are generated are effectively suppressed by using the new sensor.

The streamwise variations of density along the line passing through the vortex core are compared in Figure 5. The use of the proposed sensor removes not only the two-point oscillations but also the numerical oscillations of lower wavenumbers that are generated as the hybrid solver responds to the two-point oscillations. Other than these, the density fields are similar to each other and are comparable in terms of captured features with the solutions from earlier studies [6, 7]. Lo and coworkers [6] predict a thinner shock by clustering the grid in the axial direction around the shock.

(a) with Gibbs phenomenon detector   (b) without Gibbs phenomenon detector
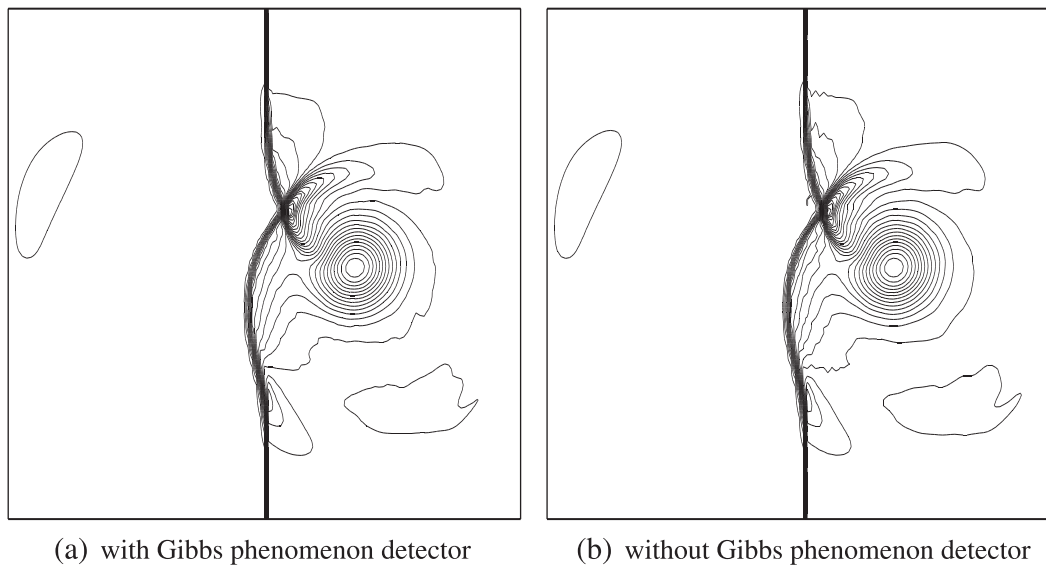
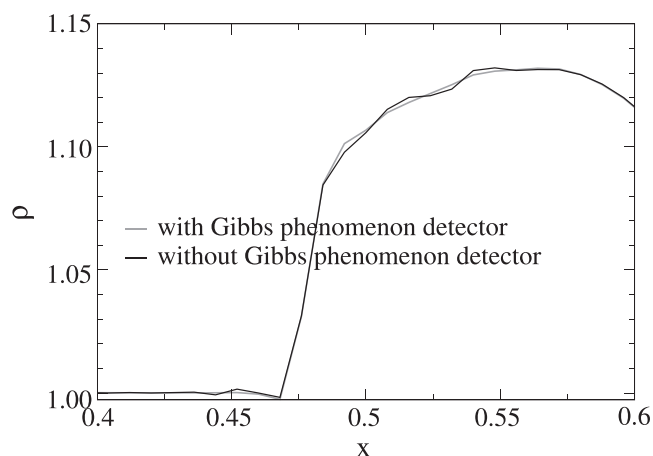Figure 4. Density isolevels for the shock–vortex interaction problem.

Figure 5. Predicted axial density variations on the line passing through the vortex core.

3.5. LES of supersonic flow over a backward-facing step

In addition to a separation zone, this flow contains an expansion fan, a slip line, and a shock wave interacting with an unsteady vorticity field. The details of the simulation are provided in Table I. To the extent possible, the LES here are deliberately made identical to one from an earlier study [21] to facilitate comparison. This earlier study used a validated LES solver and a subgrid kinetic energy equation model, while a simpler Smagorinsky model [22] is used here. Assuming that flow settles down to a statistical stationary state after initial five flow-through times, the statistics are computed over the next 20 flow-through times. The convergence of statistics for this case is dictated by the dynamics of the recirculation zone. The simulation time (in terms of flow-through time) is unusually high in order to account for possible low-frequency dynamics.

In the reference study [21], flow through a converging–diverging nozzle was simulated to generate the inflow conditions. The mean streamwise velocity profile and the adiabatic wall temperature from it are used to specify the steady components of the streamwise velocity and temperature (from Walz equation). For unsteady components, a compressible version of the digital filtering approach [23] is used here. Half a step height upstream of the step location ($x = -H/2$ where origin corresponds

Table I. Parameters for LES of flow over backward-facing step.

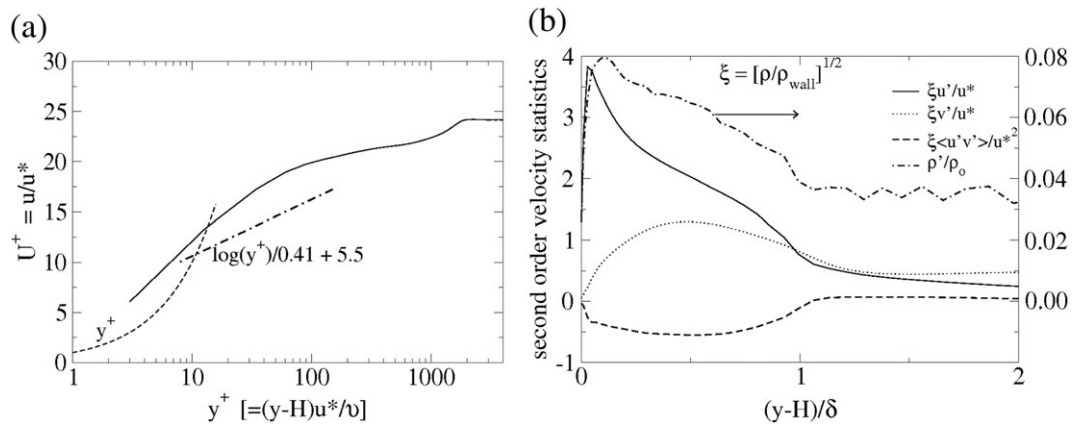|	
Free stream Mach number	1.5
Total pressure	54 psi
Total temperature	300 K
Step height (H)	0.25 in.
Domain size	9.8 H × 5.0 H × 2.0 H
Reynolds number (freestream quantities, H)	250,000
Inflow boundary layer thickness (δ_o)	0.08 in.
Distance between the inlet and the step location	1.9 H
Mesh size	240 × 140 × 64

Figure 6. Boundary layer characteristics half a step height upstream of the step. (a) Mean velocity profile in inner scaling and (b) second-order statistics in Morokovin representation in outer scaling.

to the bottom of the step location), the boundary layer predictions are plotted in Figure 6. As seen, the mean velocity profile deviates from the law of the wall. No attempt is made to satisfy the law of the wall at the inlet; the inlet velocity profile provided in the reference study is used as is. The flow may need to traverse over a longer distance for the linear and logarithmic scalings corresponding to equilibrium boundary layers to be established. Lack of sufficient near-wall resolution may also be a reason. It is also to be noted that the effect of expansion at the step could be felt upstream through the subsonic portion of the boundary layer, and so a truly equilibrium boundary layer should not be expected at this location. The boundary layer profiles of turbulent quantities at this Reynolds number and Mach number are not available in literature. Widely known trends from DNS studies [24] like peaks of velocity fluctuation levels remaining nearly unaltered but shifting closer to the wall with increasing Reynolds number indicate that fluctuation levels of streamwise velocity are overpredicted, while the Reynolds stress levels are underpredicted. Also, peaks in wall normal and Reynolds stress profiles, which are expected to be in the first quarter of the boundary layer, are closer to the middle of the boundary layer. LES-predicted peaks shift away from the wall as the grid is coarsened [25], and so the deviations here may mostly be due to low resolution. The density fluctuations profile is similar to those obtained in experiments and in LES of a 0.9 Mach number compressible boundary layer [26], while it differs from one obtained in DNS of a 2.25 Mach number boundary layer [27] that has a peak closer to the outer edge than the wall. At lower Mach numbers, the Reynolds analogy seems to hold so that the density and temperature fluctuations peak at closer locations, but as Mach number increases, both total temperature and thermodynamic pressure are no longer uniform, and so density fluctuations peak in the outer half of the boundary layer, while temperature fluctuations peak in the other.

The LES that performed with and without considering the Gibbs phenomenon detector (i.e., using Equations (6) and (4), respectively) seem to produce indistinguishable results. The contour plot of instantaneous density field from the former LES is shown in Figure 7. Unsteady disturbances that propagate along the Mach lines starting at the corner of the inlet and wall boundaries are evident. The

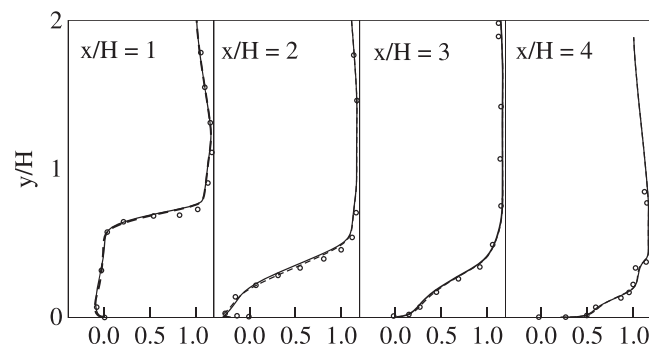Figure 7. Density field predicted using LES.

Figure 8. Predicted mean velocity profiles at various axial locations. The symbols represent predictions of reference LES [21], while solid and dashed lines correspond to predictions of present solver with and without Gibbs phenomenon detector, respectively.

transverse velocity at the inlet is set to zero, while in reality, there is an updraft from the wall. The unsteady fluctuations are also not solutions of the governing equations. These two approximations generate some unphysical disturbances that may affect the flow downstream. The earlier study does not have this problem because a precursor simulation was used to supply the inlet conditions. Other than this artifact, all other features are similar in both studies.

The mean reattachment length turns out to be 2.98 H when the Gibbs phenomenon detector is used and 2.97 H when it is not. Ayyalasomayajula and coworkers [21] reported a prediction of 2.82 H from their LES as compared with the experimental value of 3.0 H. If uncorrelated random fluctuations are used to specify the inlet turbulence, the reattachment length predicted is about 4.3 H. The shear layer instability at the step corner and subsequent breakdown are delayed because of lack of large-scale structures in the flow when random noise is used. This delayed reattachment results in a larger recirculation bubble. The use of random noise for inflow also leads to an overprediction of the reattachment length in the subsonic case as well [28], but the 43% error seems much higher in the supersonic case here.

The mean velocity predictions from both simulations shown in Figure 8 agree very well with those from the reference study. The Gibbs phenomenon detector has no impact probably because the shock is relatively weak and the slip line is parallel to the flow direction. Other important observation is that the digital filtering approach generates a spectrum of eddies that trigger the shear layer instability as needed.

The Gibbs phenomenon detector has no effect on the turbulent intensities as well as seen in Figure 9. The simulations here overpredict the levels by about 15% compared with the reference study except at the first location. The exact reason for this is not clear. Examination of contour plots indicates the present resolution may be lower than in the earlier study. This, in addition to the difference in subgrid modeling, could be a possible reason. The unphysical noise generated at the
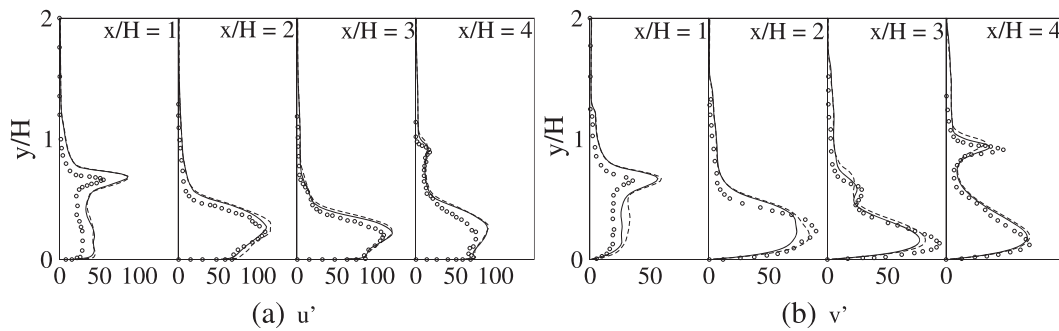
Figure 9. Predictions of turbulent intensity profiles at various axial locations. Symbols represent predictions of reference LES [21]; dotted and solid lines represent LES predictions made without and with Gibbs phenomenon detector.
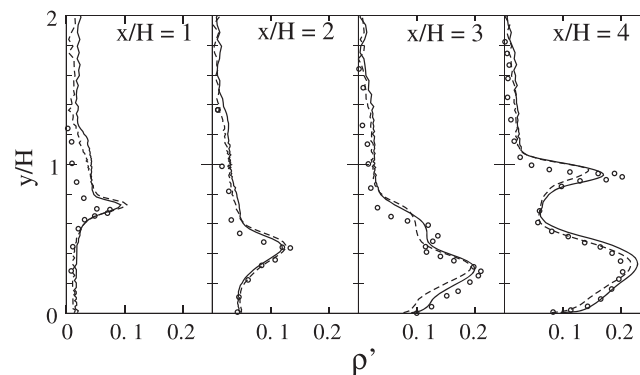

Figure 10. Predicted density fluctuations at various axial locations. The symbols represent predictions of reference LES [21], while solid and dashed lines correspond to predictions of present solver with and without Gibbs phenomenon detector.

inflow (Figure 7) could also generate higher unsteadiness in the flow as it propagates through the expansion fan at the corner.

Shown in Figure 10 are profiles of density fluctuations at the same four axial locations as in previous plots. At the first location, the fluctuation levels do not drop to zero above the shear layer created by boundary layer crossing the step. As stated previously, the unphysical pressure disturbances generated at the corner of the inflow boundary and the lower wall travel along Mach lines and disturb the flow outside the boundary layer. Other noteworthy feature is that the sharper peak at the last axial locations seems slightly better predicted when the Gibbs phenomenon sensor is used. This peak results from the unsteady fluctuations of the reattachment shock. The prediction of the corresponding peak in transverse velocity fluctuations also improves with the use of the new detector.

3.6. LES of a transonic boundary layer over a bump

The LES of an equilibrium transonic turbulent boundary layer passing over a circular arc-shaped bump are performed to test the newly proposed sensor. Sandham and coworkers [29] have reported an LES of this flow, and the same parameter set is used here to the extent possible so that their results can be used for comparison. The flow/simulation parameters are listed in Table II. All listed length scales are based on the inlet boundary layer displacement thickness (set to unity) as a reference.

The domain and mesh used for the simulation viewed from spanwise direction are shown in Figure 11. The grid lines bend sharply above the corners at the start and the end of the bump, and no attempt is made to smoothen the mesh so as to be consistent with the mesh used in the reference study [29]. The mesh used here is coarser, but near-wall grid spacing in wall normal direction is

Table II. Parameters for LES of a transonic boundary layer over a bump.

Free stream Mach number	0.72
Exit pressure/inlet stagnation pressure	0.65
Inlet temperature	300 K
Bump base, height	80, 5
Domain size	$240 \times 62.5 \times 16$
Radius of curvature of the arc	163
Inflow boundary layer thickness	7.7
Mesh size	$390 \times 100 \times 48$
Min grid spacings in wall units	44, 0.67, 22
Reynolds number (freestream and bump base)	233,000
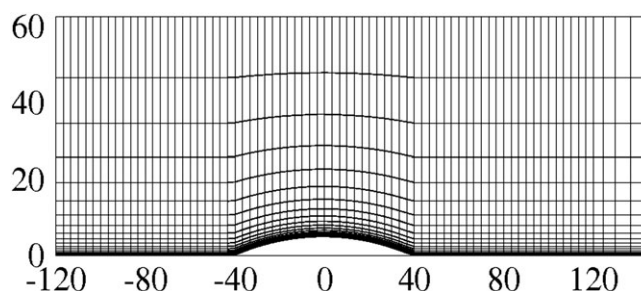
Figure 11. Grid used for the LES of transonic flow over a bump viewed on the $X-Y$ plane (every fifth grid line is shown).

ensured to be less than unity in wall units. Thirty additional points in the streamwise direction are added, and the grid is stretched out rapidly to create a sponge zone so that disturbances at the outflow boundary do not propagate in and contaminate the solution in the domain of interest. The simulation is conducted for 16 flow-through times, but the predictions from the latter half are used for computing the statistics reported here. As in the reference study, the flow is assumed to settle down to a statistically stationary state after eight flow-through times.

No-slip boundary conditions are used at the solid boundaries. Wall temperature is specified to be equal to the inflow stagnation temperature. Periodic and free-slip boundary conditions, respectively, are used in the spanwise direction and the top boundary. Zero-gradient conditions for density and velocity fields and a fixed-back pressure are used at the outflow boundary. The digital filtering approach is used for specifying the inlet turbulence. Sandham and coworkers had used the synthetic turbulence approach [29] but subsequently established that digital filtering leads to faster realization of a turbulence and slightly better second-order moments [23]. Specifically, the synthetic turbulence approach creates an additional peak in streamwise intensity in addition to the near-wall peak.

The predicted profiles of mean velocity and turbulent fluctuations at $x = -80$ are shown in Figure 12. This location is halfway between the inlet and the bump, and the flow has traversed a distance equaling 40 times the displacement thickness from the inlet. This distance was used in the simulation for testing their inflow generation technique by Sandham and coworkers [29]. The profile seems to approach the law of the wall relatively quickly given that the inflow profile was specified on the basis of outer scaling only. The normal components of the stress tensor are very close to their equilibrium levels. The Reynolds stress levels drop drastically close to the inlet (as seen from the profile at $x = -110$), but peak level seems to recover to within 20% of expected value at $x = -80$ (note that the peak level of Reynolds stress is typically around $-0.9u^{*2}$ in boundary layers, where u^{*2} is the friction velocity). Complete recovery can be expected to happen given that flow has to travel nearly seven more boundary layer widths before encountering the bump.

Although the filtering operation in the digital filtering technique mostly creates eddies that are well resolved on the mesh, two-point oscillations can still be generated. The use of the Gibbs phenomenon detector in the solver can result in additional dissipation that would not otherwise exist if
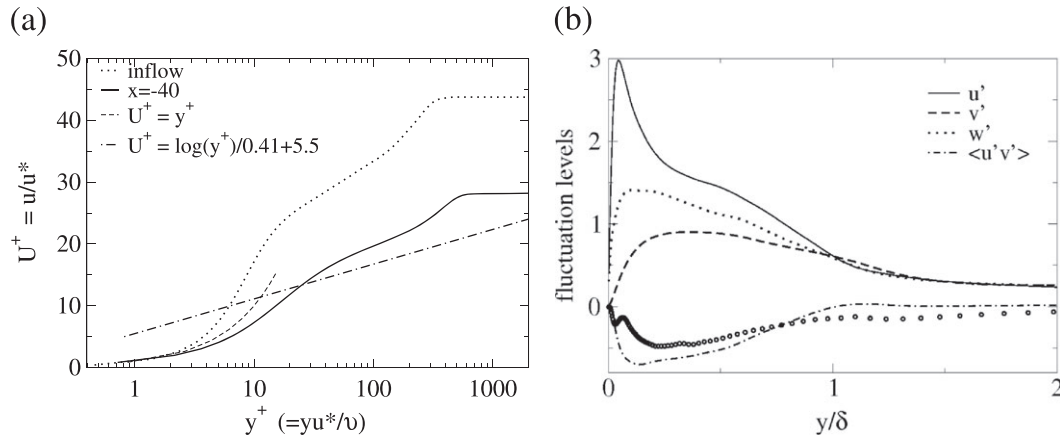
Figure 12. Boundary layer characteristics at $x = -80$ (midway between inflow and the bump). (a) Mean velocity profile in inner scaling and (b) second-order statistics in outer scaling. The symbols denote Reynolds stress profile at $x = -110$, which is included here to show a steep drop in Reynolds stress level next to the inlet. Change in profiles between $x = -110$ and $x = -80$ indicate the level of recovery towards an equilibrium level.
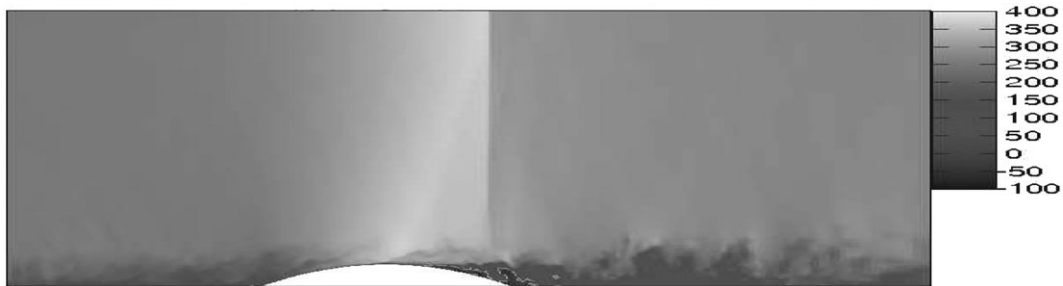

Figure 13. Instantaneous velocity field predicted with the proposed approach. Isolevel indicating zero velocity shows two separate zones of reverse flow near the wall.

it is not used. The process of generating a realistic boundary layer from inlet turbulence, therefore, depends on whether the new sensor is used or not. In order to avoid drift between the two LES, the sensor is used in both of them till $x = -70$. Downstream of this location, the sensor is used in only one of the simulation. This way, the bump encounters similar flows that are free of poorly resolved two-point oscillations in both simulations. Comparison of the predictions downstream of this location (above and downstream of the bump) is then a true test of how well the unphysical oscillations, whatever their genesis maybe, are controlled by the proposed approach.

The instantaneous streamwise velocity field predicted using the proposed approach is visualized in Figure 13. A zero isolevel contour shows two separated negative velocity zones indicating a smaller recirculation bubble before a large one further downstream. This feature is missing if only a conventional discontinuity sensor is used. This is also evident in the skin friction coefficient plot discussed later.

The Mach number predictions on the slip boundary are compared with those from the reference LES in Figure 14. The shock locations are predicted to be slightly upstream of the previous LES prediction ($x = 32$). The preshock (peak) Mach numbers turns out to be 1.147 when the new sensor is used, and it is slightly lower (1.146) when it is left out. The value predicted in previous LES is 1.16. So the shocks are slightly weaker in the present study. The pressure predictions along the solid wall are compared with the corresponding predictions from the reference LES in Figure 15(a). Both predictions in the present study seem quite similar but differ from those of previous LES presumably because of differences in predictions of separation zone dynamics. A zoomed-in view of the same plot near the upstream corner of the bump is shown in Figure 15(b). The compression of the flow
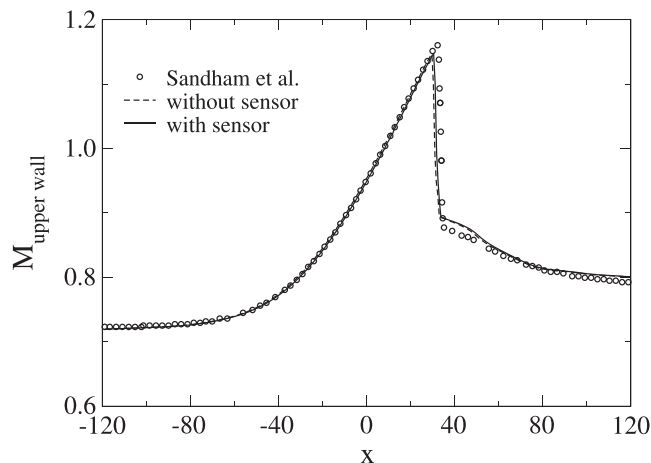
Figure 14. Freestream Mach number variation in the transonic flow over a bump.

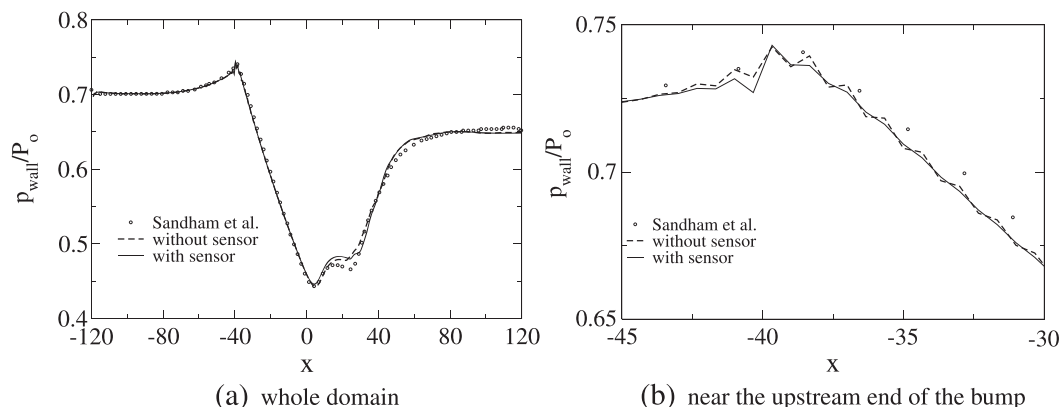
(a) whole domain

(b) near the upstream end of the bump

Figure 15. Prediction of pressure on the solid wall.

along with the abrupt changes in mesh metrics generates numerical two-point oscillations at the corner. When the new sensor is used, these are properly sensed and localized through the use of additional dissipation.

The predicted skin friction coefficient variations along the lower wall are plotted in Figure 16. The freestream stagnation speed of sound and stagnation density are used as reference quantities to non-dimensionalize the wall shear stress just as in case of the reference study [29]. Use of the new sensor seems to have a noticeable effect, especially on the post-separation dynamics. When the proposed sensor is used, the flow separates around $x = 11$, reattaches (roughly around $x = 20$), and then at the foot of the shock separates again. Otherwise, only one recirculation zone (between $x = 12$ and $x = 49$) is predicted.

Comparison with results from previous LES is not made for the following reasons. The skin friction coefficient of the approaching boundary layer seems to settle down to a value between 0.0005 and 0.0006 before encountering the bump in that study, while in the present study, it is nearly double. If the freestream values are used for non-dimensionalization while computing C_f, the values in the figure would need to be scaled by a factor of 2.63. When this scaling is applied, the approaching boundary layer asymptotes to a value around 0.0031. This is nearly the value obtained when the DNS predictions of Spalart [24] are extrapolated to the momentum thickness-based Reynolds number of the boundary layer here.

Not only the quantitative values but even the trends in the axial profiles of skin friction coefficient differ between the two studies. If the shear stress is non-dimensionalized using the local density instead of stagnation density, the resulting profile from the LES with the new sensor appears
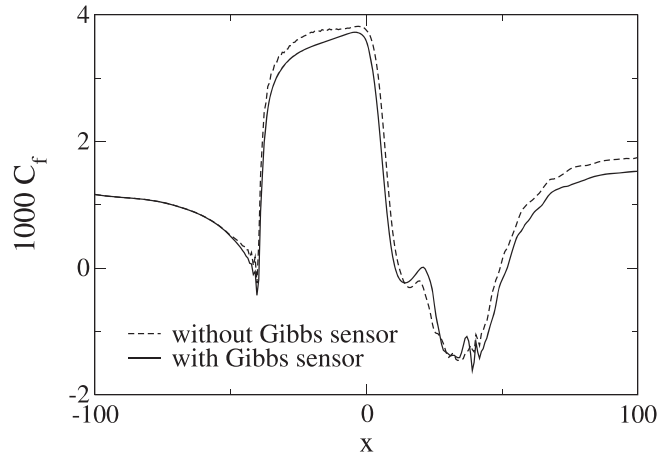
Figure 16. Friction coefficient on the lower wall. Freestream stagnation quantities are used as reference values.
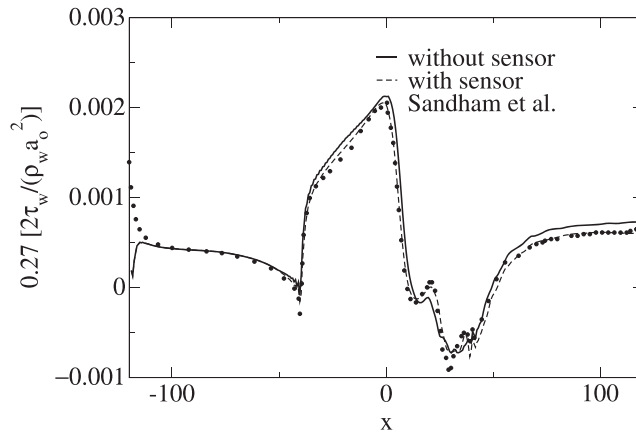

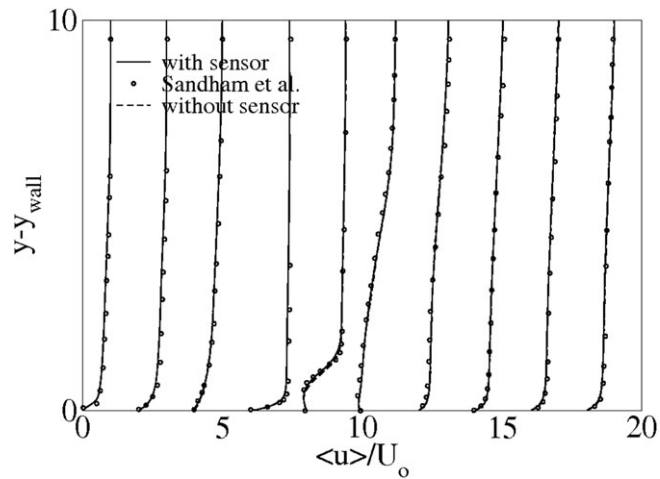Figure 17. Normalized shear stress on the wall.

Figure 18. Cross-stream profiles of mean streamwise velocity at $x = -120, -80, -40, 0, 20, 40, 60, 80, 100, 120$ (profiles are in the order listed from left to right).
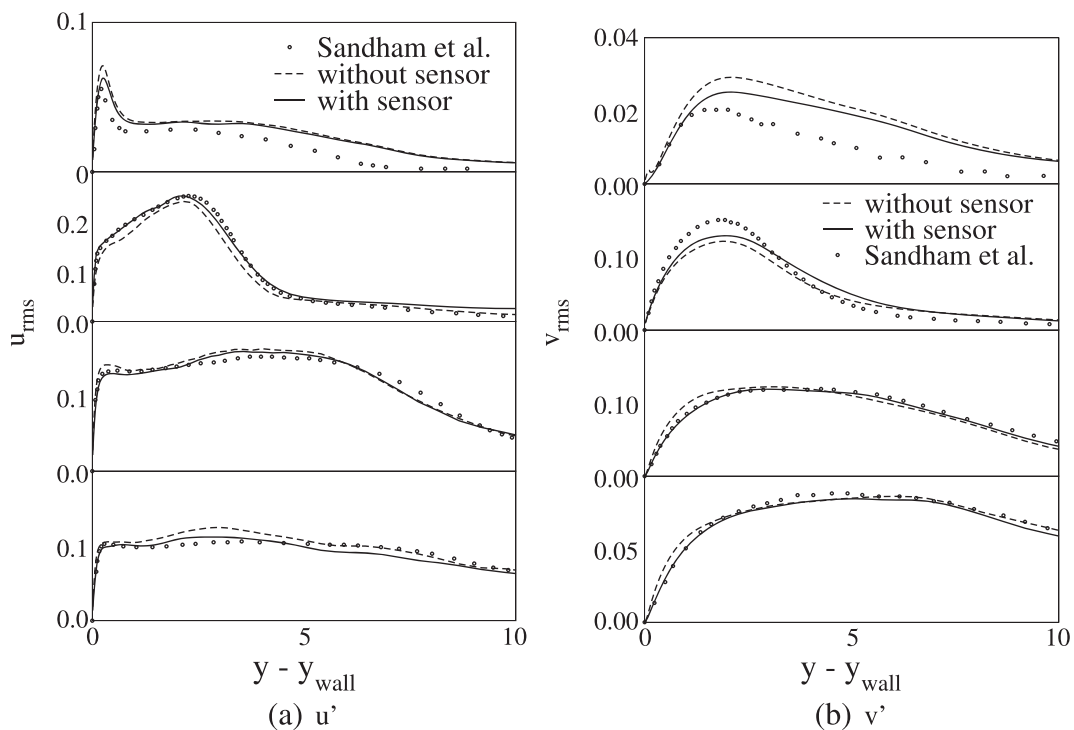
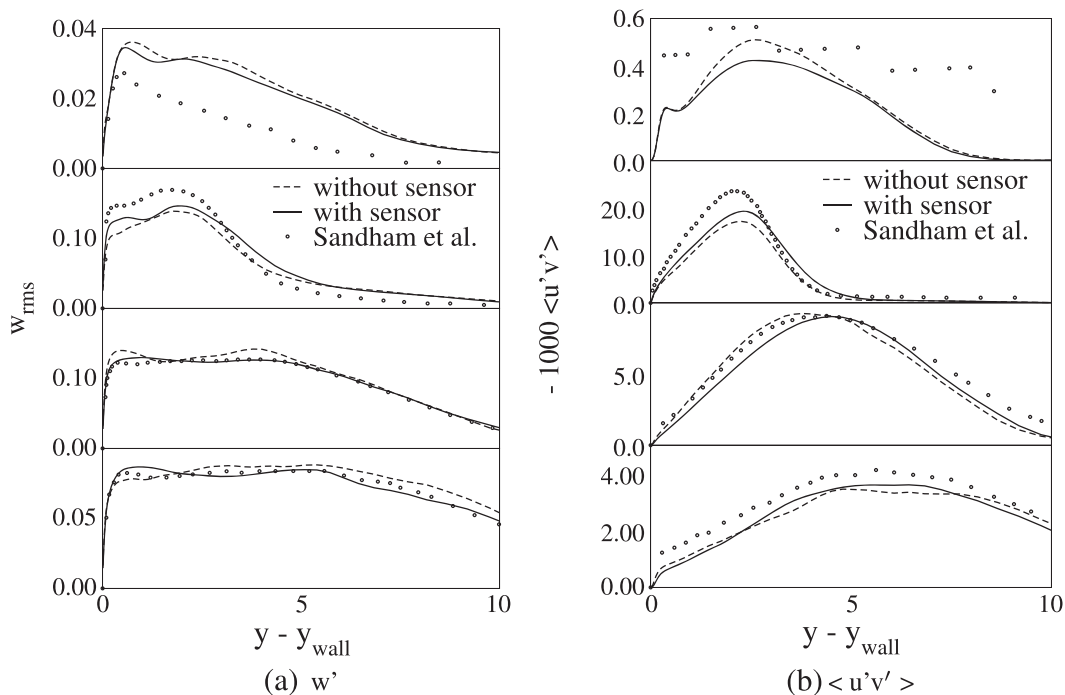Figure 19. Streamwise and cross-stream fluctuations at $x = 0, 30, 60, 100$.

Figure 20. Spanwise fluctuations and Reynolds stresses at $x = 0, 30, 60, 100$.

qualitatively very similar to the one from previous LES. In fact, when scaled appropriately, the former profile matches almost exactly with the latter as shown in Figure 17. If the possibility of a coincidence is ruled out, this plot serves as a validation for the approach proposed here.

Figure 18 shows the predicted velocity profiles along the cross-stream direction at various axial locations. The predictions with and without the sensor (i.e., using Equation (4)) are almost indistinguishable and also differ little from the corresponding predictions of previous LES except perhaps at two locations on either sides of the separation point ($x = 20, 40$). The cross-stream profiles of second-order velocity statistics at four of the axial locations are shown in Figures 19 and 20. The freestream stagnation speed of sound is used to non-dimensionalize the fluctuation levels. Except on the very top of the bump, the predictions of both LES here match quantitatively well with those from the earlier study. The differences in axial and spanwise resolutions could be one likely reason why the reduction in turbulence levels due to compression differs between the two studies, although the differences in predictions of the two LES here are minor but more noticeable than in the previous test case and those generated using the sensor are marginally closer to reference data from previous LES.

4. CONCLUSIONS

Inclusion of a simple Gibbs phenomenon detector in the hybridization is effective in suppressing numerical oscillations in canonical tests and LES. The key feature of this approach is the integrated treatment for numerical oscillations both near and far away from discontinuities. It, however, does not seem to affect the results in the LES of supersonic flow over a backward-facing step because the shock is quite oblique and the slip line is parallel to the flow. The use of Gibbs phenomenon detector does not seem to have added any additional numerical dissipation in this test case. The LES results for the transonic flow over a bump, on the other hand, change noticeably if the new sensor is used to determine the weights for combining the central and Riemann fluxes. The non-smooth variations in grid metrics near the corners create two-point numerical oscillations that prompt the new sensor to respond by increasing the weight of the Riemann flux. Also, the turbulence inside the boundary layer is interacting with a normal shock in this case. When the proposed sensor is included, the separated flow on the downstream side on the bump reattaches and then separates again at the foot of the shock creating two separation bubbles just as in the LES of Sandham and coworkers [29]. Without this sensor, there is only one large separation bubble. Comparisons with previous LES show that the additional dissipation due to the use of the new sensor is not detrimental for capturing turbulence while being effective in localizing the numerical oscillations.

The proposed strategy to control numerical oscillations seems most useful when the shock waves are normal to the turbulent flow as seen from the Emery test and the second LES presented here. LES solutions in the latter are affected when the new numerical oscillation sensor is used in the hybridization even though the shock is quite weak. This sensor can be expected to lead to more substantial changes in the solution when the normal shock is stronger. This happens in flows with crossflow injections into supersonic boundary layers. The incoming boundary layer encounters the leading edge of the shock at a right angle, a situation somewhat similar to one seen in the Emery test case. The future work involves testing the new sensor for such a flowfield.

REFERENCES

1. Pirozzoli S. Conservative hybrid compact-WENO schemes for shock–turbulence interaction. *Journal of Computational Physics* 2002; **178**:81–117.
2. Genin F. Study of compressible turbulent flows in supersonic environment by large eddy simulation. *Ph.D. Thesis*, Georgia Institute of Technology, Atlanta, GA, USA, 2009.
3. Pirozzoli S, Bernardini M, Grasso F. Direct numerical simulation of transonic shock/boundary layer interaction under conditions of incipient separation. *Journal of Fluid Mechanics* 2010; **657**(1):361–393.
4. Cook AW, Cabot WH. Hyperviscosity for shock–turbulence interactions. *Journal of Computational Physics* 2005; **203**:379–385.
5. Kawai S, Lele SK. Localized artificial diffusivity scheme for discontinuity capturing on curvilinear meshes. *Journal of Computational Physics* 2008; **227**:9498–9526.
6. Lo SC, Blaisdell GA, Lyrintzis AS. Higher-order shock capturing schemes for turbulence calculations. *AIAA paper 2007-827* 2007.

7. Guo-Hua T, Xiang-Jiang Y. A characteristic-based shock-capturing scheme for hyperbolic equations. *Journal of Computational Physics* 2007; **225**:2083–2097.
8. von Kaenel, Kleiser L, Adams NA, Vos JB. Large-eddy simulation of shock–turbulence interaction. *AIAA Journal* 2004; **42**(12):2516–2528.
9. Johnsen E, Larsson J, Bhagatwala AV, Cabot WH, Moin P, Olson BJ, Rawat PS, Shankar SK, Sjogreen B, Yee HC. Assessment of high resolution methods for numerical simulations of compressible turbulence. *Journal of Computational Physics* 2010; **229**:1213–1237.
10. Pirozzoli S. Numerical methods for high-speed flows. *Annual Review of Fluid Mechanics* 2011; **43**:163–194.
11. Chakravarthy VK, Arora K, Chakraborty D. A simple hybrid finite volume solver for compressible turbulence. *International Journal for Numerical Methods in Fluids* 2015; **77**(12):707–731.
12. Nishikawa H, Kitamura K. Very simple, carbuncle-free, boundary-layer-resolving, rotated-hybrid Riemann solvers. *Journal of Computational Physics* 2008; **227**:2560–2581.
13. Shima E, Kitamura K. Parameter-free simple low-dissipation AUSM-family scheme for all speeds. *AIAA Journal* 2011; **49**(8):1693–1709.
14. Chakravarthy VK, Chakraborty D. Modified SLAU2 scheme with enhanced shock stability. *Computers and Fluids* 2014; **100**:176–184.
15. Rhie CM, Chow WL. A numerical study of the turbulent flow past an isolated airfoil with trailing edge separation. *AIAA Journal* 1983; **21**(11):1525–1532.
16. Adams NA, Shariff K. A high-resolution hybrid compact-ENO scheme for shock–turbulence interaction problems. *Journal of Computational Physics* 1996; **127**:27–51.
17. Fiorina B, Lele SK. An artificial nonlinear diffusivity method for shock-capturing in supersonic reacting flows. *Technical Report 57-70*, Annual Research Briefs, Center for Turbulence Research, Stanford University: CA, USA, 2005.
18. Liska R, Wendroff B. Comparison of several difference schemes on 1D and 2D test problems for the Euler equations. *SIAM Journal on Scientific Computing* 2003; **25**:995–1017.
19. Toro EF. *Riemann Solvers and Numerical Methods for Fluid Dynamic* (Third edn.) Springer-Verlag: Berlin, Germany, 2009.
20. Emery AE. An evaluation of several differencing methods for inviscid fluid flow problems. *Journal of Computational Physics* 1968; **2**:306–331.
21. Ayyalasomayajula H, Arunajatesan S, Kannepalli C, Sinha N. Large eddy simulation of a supersonic flow over backward-facing step for aero-optical analysis. *AIAA paper 2006-1416* 2006.
22. Smagorinsky J. General circulation experiments with the primitive equations. *Monthly Weather Review* 1963; **91**:99–164.
23. Touber E, Sandham ND. Large-eddy simulation of low frequency unsteadiness in a turbulent shock-induced separation bubble. *Theoretical and Computational Fluid Dynamics* 2009; **23**:79–107.
24. Spalart P. Direction numerical simulation of turbulent boundary layer up to $Re_\theta = 1410$. *Journal of Fluid Mechanics* 1988; **187**:61–98.
25. Spyropoulos ET, Blaisdell GA. Large-eddy simulation of a spatially evolving supersonic turbulent boundary-layer flow. *AIAA Journal* 1998; **36**(11):1983–1990.
26. Tromeur E, Gariner E. Analysis of the Sutton model for aero-optical properties of compressible boundary layers. *Journal of Fluids Engineering* 2006; **128**:239–246.
27. Pirozzoli S, Grasso F, Gatski TB. Direct numerical simulation and analysis of a spatially evolving supersonic turbulent boundary layer at $m = 2.25$. *Physics of Fluids* 2004; **16**(3):530–545.
28. Panjwani B, Ertesvag IS, Gruber A, Rian KE. Large eddy simulation of backward facing step flow. *5th National Conference on Computational Mechanics, MekIT09*, Trondheim, Norway, 2009.
29. Sandham ND, Yao YF, Lawal AA. A large eddy simulation of transonic turbulent flow over a bump. *International Journal of Heat and Fluid Flow* 2003; **24**:584–595.